C. R. Physique 18 (2017) 57–65

Contents lists available at ScienceDirect

Comptes Rendus Physique

www.sciencedirect.com

Snowpack permittivity profile retrieval from tomographic SAR data

Badreddine Rekioua [a,b,**,1], Matthieu Davy [b,*], Laurent Ferro-Famil [c,*], Stefano Tebaldini [b]

[a] IETR UMR CNRS 6164, Université de Rennes-1, 35000 Rennes, France
[b] Ecole militaire polytechnique de Bordj El Bahri, 16111, Alger, Algeria
[c] Dipartimento di Electronica, Informazione e Bioingegneria, Politecnico di Milano, 20133 Milano, Italy

ARTICLE INFO

Article history:
Received 24 August 2015
Accepted 1 December 2015
Available online 19 February 2016

Presented by M. Denis Gratias

Keywords:
Snowpack
Snow permittivity
SAR
SAR tomography
GB-SAR
Time domain back projection

ABSTRACT

This work deals with 3D structure characterization and permittivity profile retrieval of snowpacks by tomographic SAR data processing. The acquisition system is a very high resolution ground based SAR system, developed and operated by the SAPHIR team, of IETR, University of Rennes-1 (France). It consists mainly of a vector network analyser and a multi-static antenna system, moving along two orthogonal directions, so as to obtain a two-dimensional synthetic array. Data were acquired during the AlpSAR campaign carried by the European Space Agency and led by ENVEO. In this study, tomographic imaging is performed using Time Domain Back Projection and consists in coherently combining the different recorded backscatter contributions. The assumption of free-space propagation during the focusing process is discussed and illustrated by focusing experimental data. An iterative method for estimating true refractive indices of the snow layers is presented. The antenna pattern is also compensated for. The obtained tomograms after refractive index correction are compared to the stratigraphy of the observed snowpack.

1. Introduction

SAR imaging systems provide large-scale and high-resolution imaging capabilities, independently of day–night and weather conditions. A conventional SAR projects a *3D* reflectivity map on a *2D* plane. This projection from *3D* to *2D* space induces some effects like layover and foreshortening [1]. For some applications like urban area and natural environment monitoring, *2D* SAR imaging comes to be of a limited interest by omitting the description of the vertical structure of the observed scene. This limitation is a serious shortcoming for the special case of snow cover monitoring applications, like hazard forecasting, water resource management, and climate change monitoring. Indeed, for these applications, an accurate description of the vertical structure of the snow cover is of great interest [2]. Many works have addressed the problem of

* Corresponding authors.
** Principal corresponding author at: IETR UMR CNRS 6164, Université de Rennes-1, 35000 Rennes, France.
E-mail addresses: badreddinerekioua@gmail.com (B. Rekioua), matthieu.davy@univ-rennes1.fr (M. Davy), Laurent.Ferro-Famil@univ-rennes1.fr (L. Ferro-Famil), stefano.tebaldini@polimi.it (S. Tebaldini).
[1] B. Rekioua is a Phd student of the IETR of University of Rennes 1 (France) with a scholarship from the Military Polytechnical School of Bordj El Bahri (Algiers, Algeria).

http://dx.doi.org/10.1016/j.crhy.2015.12.016
1631-0705/

Fig. 1. GB-SAR system of the SAPHIR team of the University of Rennes-1.

Table 1
Main characteristic of the GB-SAR system.

Freq. band	X, Ku
Vertical resolution [cm]	∼4 (Ku band) ∼10 (X band)
Range resolution [cm]	∼4
Azimuth resolution [cm]	∼2
Polarization	VV, HV

assessing the physical properties of snow covers using SAR data. Mainly, SAR data are used to estimate snow wetness [3–6], snow water equivalent [7–10], snow depth [11–13], snow density [14,15] or snow covered areas [16,17]. For the above cited works, one or more parameters of snow covers are investigated without addressing directly the vertical structure of the observed scenes which may relate into ambiguous interpretations or ill-conditioned estimation. In this context, SAR tomography (TomSAR) represents a promising tool for monitoring snow and ice due to its ability of resolving *3D* scatterer contributions and therefore overcoming layover and foreshortening effects [18,19]. In this work, the description of the vertical structure of a snowpack using TomSAR data is addressed by retrieving the vertical permittivity profile that represents a key information for estimating the physical parameters. The processed data were acquired using a Ground Based SAR (GB-SAR) system developed and operated by the SAPHIR team, of the IETR of the University of Rennes-1 in the framework of the European Space Agency (ESA) AlpSAR campaign led by ENVEO in the Austrian Alps. The GB-SAR system was operated at both X and Ku bands, allowing for resolutions within a few centimeters. The processing of the acquired data is done using the Time Domain Back Projection Algorithm (TDBPA). The resulting tomograms show an overestimation of snowpack height and geometrical distortions. These distortions are caused by the implicit assumption of free space propagation during the focusing process. In order to have a correct interpretation of the obtained tomograms, the focusing algorithm must take into account the correct permittivities, unknown *a priori*. An iterative procedure is proposed to estimate the correct permittivity for each snow layer and the corresponding thickness. Results are discussed and compared to *in-situ* stratigraphic measurements made available by ENVEO.

2. GB-SAR system and data volume description

The acquisition system is a Stepped Frequency Continuous Waves (SFCW) GB-SAR, developed, implemented, and operated by the SAPHIR team of the University of Rennes-1 (France). It comprises four rectangular horn antennas fixed at different elevation positions and connected to a Vector Network Analyser (VNA, see Fig. 1). The four antennas and the VNA hold on a metallic box mounted on a 3 m-long rail equipped with a linear stepper motor. Each antenna can operate either as a transmitter or a receiver resulting in six equivalent monostatic antenna positions with constant spacing in the elevation direction. More elevation positions can be obtained by changing the position of the antenna array on the metallic box or by changing the elevation of the rail. The ground coverage of the GB-SAR is limited by the rail height and the antennas' radiation pattern. The system and data storage are controlled by a laptop computer. The parameters describing each data acquisition are the transmitted frequency, the combination of the transmitting and receiving antennas as well as their azimuth position. Acquisitions are performed in the X and Ku frequency bands with a bandwidth $B_f = 4$ GHz. The corresponding range resolution is given by Eq. (1):

$$\delta_r = \frac{c}{2\,B_f} = 3.75\ [\text{cm}] \tag{1}$$

The GB-SAR is a high resolution *3D* imaging system with a few centimeters resolution in elevation, ground range and azimuth directions. Its main characteristics are summarized in Table 1.

The processed data were acquired during the ESA AlpSAR campaign led by ENVEO in the Austrian Alps. The snowpack measured at the Rotmoos test site is composed of a stack of horizontal snow slabs, with a total height of about 137 cm. Its structure is depicted by the profile given in the panel on the right in Fig. 10, which provides the different physical parameters (see Table 2) as a function of snow depth.

Table 2
Definition of the physical parameters used to describe snow stratigraphy.

Symbol	Definition
H [cm]	Height from the base
F	Shape description
E [cm]	Average grain size
$E_{\max}$ [cm]	Average maximum grain size
R	Snow hardness description
HW [kg·m^{-2}]	Snow water equivalent
ρ [kg·m^{-3}]	Snow density

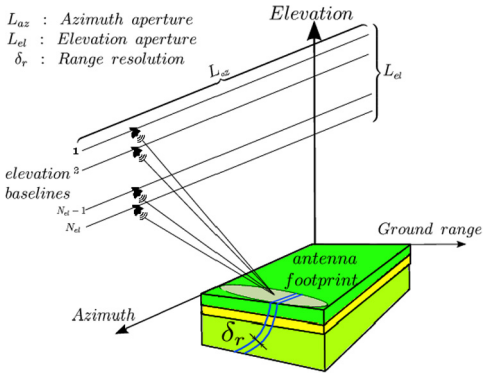

Fig. 2. TomSAR recording configuration.

3. Data processing

3.1. 3D focusing

SAR Tomography exploits multiple passes operated over the elevation direction to achieve a focusing capability along the elevation direction [20] (see Fig. 2). The response of a point target at position $\vec{r}$ seen by the GB-SAR is expressed by:

$$s(\vec{r}-\vec{p},k)=\frac{\exp(-\mathrm{i}k\,\|\vec{r}-\vec{p}\|)}{\|\vec{r}-\vec{p}\|}\,\tilde{\sigma}(\vec{r}-\vec{p},k)\,U(\vec{r}-\vec{p},k) \tag{2}$$

Here $k=\frac{4\pi}{\lambda}$ is the wavenumber, $\vec{p}$ is the transmitting–receiving antennas position and $U(\vec{r}-\vec{p})$ is the transmitting–receiving antenna gain, $\tilde{\sigma}(\vec{r}-\vec{p},k)$ is the complex response of the target.

Assuming a constant medium response over the frequency bandwidth and over the antenna positions, Eq. (2) can be written as:

$$s(\vec{r}-\vec{p},k)=\frac{\exp(-\mathrm{i}k\,\|\vec{r}-\vec{p}\|)}{\|\vec{r}-\vec{p}\|}\,\tilde{\sigma}(\vec{r}-\vec{p})\,U(\vec{r}-\vec{p}) \tag{3}$$

The total response recorded by an antenna couple at position $\vec{p}$ is given by Eq. (4):

$$S(\vec{p},k)=\int_{\Omega} s(\vec{r}-\vec{p},k)\,\mathrm{d}\vec{r} \tag{4}$$

GB-SAR data are focused using Time Domain Back Projection (TDBP). The echoes recorded by a transmitting–receiving antenna couple are correlated with the ideal response of a target at a given position $\vec{r_0}$ to get the range-focused signal expressed by Eq. (5):

$$S_r(\vec{r_0},\vec{p})=\int_{\mathrm{B_k}} S(\vec{p},\vec{k})\exp(-\mathrm{i}k\,\|\vec{r_0}-\vec{p}\|)\,\mathrm{d}k \tag{5}$$

Here $S(k,\vec{p})$ is the response recorded by a transmitting–receiving antenna couple at position $\vec{p}$, k is the wavenumber, and $\|\vec{r_0}-\vec{p}\|$ is the geometric distance between the investigated point and the emitting–receiving antenna couple.

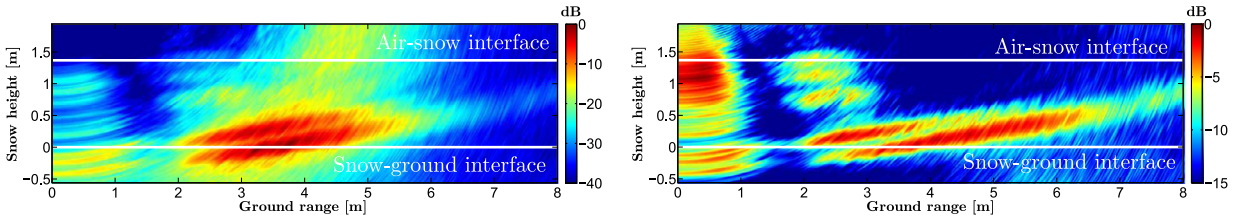

Fig. 3. Focused and multilooked tomogram. The panel on the left is the intensity image and the panel on the right is the coherency image.

The requested resolution in the ground range and elevation is then achieved by combining coherently the range focused signals at different elevation positions and different azimuth positions as follows:

$$I(\vec{r_0}) = \left| \sum_{n_z=1}^{N_{el}} \sum_{n_x=1}^{N_{az}} S_r(\vec{r_0}, \vec{p}(n_z, n_x)) \right|^2 \tag{6}$$

The coherency of the image is defined as the ratio of the coherent sum of the contributions of the different antennas $I(\vec{r_0})$ to the non-coherent sum over elevation contributions, which is the sum of the absolute values of those contributions:

$$CR(\vec{r_0}) = \frac{\sqrt{I(\vec{r_0})}}{\sum_{n_z=1}^{N_{el}} \left| \sum_{n_x=1}^{N_{az}} S_r(\vec{r_0}, \vec{p}(n_z, n_x)) \right|} \tag{7}$$

In the case of a Stepped Frequency Continuous Wave (SFCW) SAR, $S_r(\vec{r_0}, \vec{p})$ is formulated as a discrete sum over the available wavenumber bins. For N_k equidistant wavenumber bins ranging from $k_{\min}$ to $k_{\max}$ (with a step equal to Δk), the range-focused signal can be expressed as:

$$\begin{aligned} S_r(\vec{r_0}, \vec{p}) &= \sum_{n_k=0}^{N_k-1} S(n_k, \vec{p})\, e^{i(k_{\min}+n_k \Delta k)\, \|\vec{r_0}-\vec{p}\|} \\ &= e^{i k_{\min} \|\vec{r_0}-\vec{p}\|} \sum_{n_k=0}^{N_k-1} S(n_k, \vec{p})\, e^{i n_k \Delta k \|\vec{r_0}-\vec{p}\|} \end{aligned} \tag{8}$$

Equation (8) may then be slightly modified in order to account for the fact that the VNA delivers baseband signals, i.e. signals whose spectrum is demodulated around the null frequency:

$$S_r(\vec{r_0}, \vec{p}) = e^{i k_c \|\vec{r_0}-\vec{p}\|} \sum_{n_k=\frac{N_k}{2}-1}^{\frac{N_k}{2}} S_{mes}(m_k, \vec{p})\, e^{i m_k \Delta k \|\vec{r_0}-\vec{p}\|} \tag{9}$$

where $\{S_{mes}(m_k, \vec{p})\}$ is the measured response around the null frequency and k_c the central wavenumber.

The sum expressed in Eq. (9) is the IFFT of $\{S_{mes}(m_k, \vec{p})\}$. This IFFT is computed over a regular distance grid ranging from 0 to $(N_k - 1) \times \delta_r$. Then, it is interpolated at each image position defined by the range distance $\|\vec{r_0} - \vec{p}\|$.

For *3D* focusing, the imaging grid is defined by a fixed azimuth slice in the elevation-ground range plane. The set of used antennas is chosen in such a way that all investigated points fall within the −3 dB azimuth aperture of the antenna pattern.

Fig. 3 shows a multilooked tomogram obtained by applying the TDBP algorithm over *25* azimuth slices. The observed snowpack is characterized by a multi-layered vertical structure. The strongest backscattering contributions are associated with internal and bottom snow layer interfaces, whereas contributions from surface and near-subsurface are barely visible on the intensity image but well highlighted on the coherency image. The surface and the near-subsurface snow interfaces appear to be horizontal, whereas the depths associated with internal ones appear to decrease with the range. Another interesting feature is that the total snowpack height estimated by the tomogram is about 160 cm, while the *in-situ* measurements give a snow height of 137 cm. This clearly brings out geometrical distortions affecting the tomogram. These distortions are caused by the assumption of free space propagation used during the focusing process and are discussed in section 3.2.

3.2. Refractive index estimation for 3D focusing

When applying TDBPA under a free-space propagation assumption, the distance $\|\vec{r_0} - \vec{p}\|$ holds for the geometric distance between the antennas couple and the investigated point. Obviously, snow cover is a medium with refractive index $n(z)$ higher than unity [21,22] and consequently the electromagnetic distance $d(\vec{r}, \vec{p})$ is different from the geometric one. In order to correct the focusing process, the correct electromagnetic distance $d(\vec{r_0}, \vec{p})$ must be used instead of the geometric one. To quantify the undergone distortions under a free space propagation assumption in a medium with a permittivity

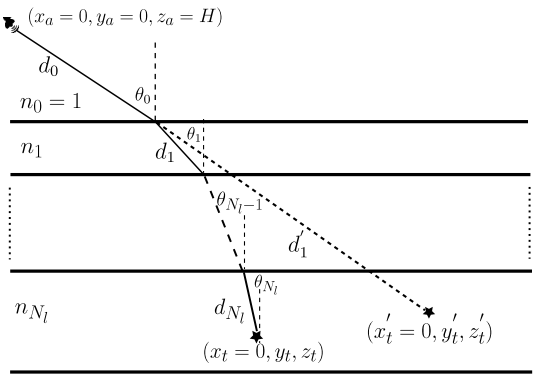

Fig. 4. Illustration of the apparent position of a target in a medium with permittivity higher than unity seen under the assumption of free-space propagation.

higher than unity, one may consider the configuration of Fig. 4. The medium is a stack of N_l homogeneous layers with permittivities $\{n_i\}$. The antenna at position $\vec{r_a} = (x_a = 0, y_a = 0, z_a = H)^{\mathbf{T}}$ records echoes from a target at position $\vec{r_t} = (x_t = 0, y_t, z_t)^{\mathbf{T}}$. The total one-way time delay from the target to the antenna is:

$$\tau = \frac{1}{c_0} \int_{\vec{r_t}}^{\vec{r_a}} n(z)\, \mathrm{d}l \tag{10}$$

In Eq. (10), c_0 is the free-space propagation speed, and $n(z)$ is the refractive index of the laterally layered medium. For the case of Fig. 4, Eq. (10) can be written as:

$$\tau = \frac{1}{c_0} \left(d_0 + \sum_{l=1}^{N_l} n_l\, d_l\right) \tag{11}$$

where d_0 is the distance traveled in the free space.

Focusing the SAR data using the geometric distance to locate image points in the range domain considers a constant velocity and a constant incidence angle within the medium (see Fig. 4). In other words, the same propagation time delay is expressed as:

$$\tau = \frac{1}{c_0} \left(d_0 + d_1'\right) \tag{12}$$

Thus, the target is seen at an apparent position satisfying $d_1' = \sum_1^{N_l} n_l\, d_l$ and the undergone distortions can be computed knowing the refraction angles $\{\theta_l\}$ and the permittivity profile $\{n_l\}$. The higher the permittivities of the medium is, the higher the distortions are. Scatterers located at far range will be affected by stronger distortions than nearer targets.

In the case of the AlpSAR campaign data, the permittivities of the observed snow covers have to be estimated. In this work, an iterative procedure for estimating refractive indices of an horizontally layered medium is introduced with application to snowpack permittivity profile retrieval. This procedure relies on the fact that the detected snow interfaces appear horizontal if the correct refractive indices are used in the focusing algorithm. This procedure iteratively estimates indices from top layers to bottom ones since the total electromagnetic distance of a target at elevation z_t depends on the refractive index profile $n(z)$, where $z \geq z_t$. One may consider a medium with three layers and four interfaces, as depicted in Fig. 5. The first interface is the air–medium interface. The second one separates layer 1 from layer 2. To estimate the refractive index of layer 1, the GB-SAR data is focused for different increasing values of refractive index n_1. For each refractive index value, the distance taking into account n_1 is computed and introduced in the TDBP algorithm. The estimated value of n_1 is chosen in such a way the second interface appears horizontal in the final tomogram. Once n_1 is fixed, the value of n_2 is estimated by focusing GB-SAR data using n_1 as refractive index for the first layer and an increasing value of n_2 until the third layer appears horizontal on the final tomogram. This procedure is repeated for each layer until all interfaces are made horizontal.

For each iteration of the correction procedure, the electromagnetic distance $d(\vec{r}, \vec{p})$ is computed. For this paper, the electromagnetic distance taking into account the different refractive indexes is computed using the eikonal equation formulation which describes the wavefront propagation through a medium defined by an isotropic varying velocity distribution. A detailed derivation of the eikonal equation can be found in Ref. [23]. The eikonal equation is:

$$\left\| \vec{\nabla} d(\vec{r}, \vec{r_a}) \right\|^2 = n^2(\vec{r}) \tag{13}$$

Equation (13) is numerically solved using the fast-marching method [24]. For the AlpSAR data, the computation of the correct electromagnetic distance on the image grid is not performed for all antenna positions. Since, the observed scene

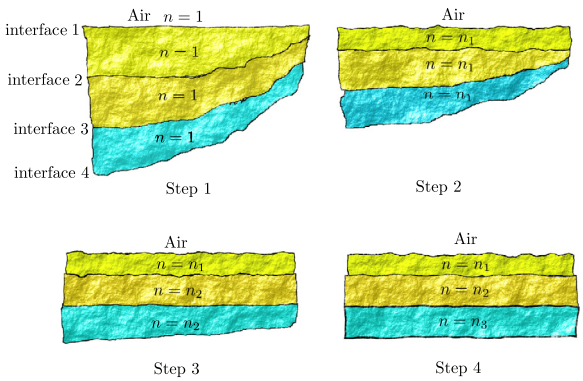

Fig. 5. Illustration of the correction steps for a 3-layer medium.

is a laterally varying medium, the z-axis is a revolution symmetry axis. Hence, the distance from an antenna position $\vec{r_a} = (x_a, y_z, z_a)^{\mathbf{T}}$ to a given target $\vec{r_t} = (x_t, y_t, z_t)^{\mathbf{T}}$ is not changed when considering an antenna at position $\vec{r_a'} = (0, 0, z_a)^{\mathbf{T}}$ and a target at position defined by Eq. (14):

$$(x_t', y_t', z_t')^{\mathbf{T}} = (0, \sqrt{(x_a - x_t)^2 + (y_a - y_t)^2}, z_t) \tag{14}$$

This remark allows us to compute the electromagnetic distance for a track n_z once over a fine grid, then the distance computation over the N_x antenna positions belonging to the n_z-th track is done by linear interpolation over a grid representing the focusing positions.

The final result after refractive index correction is shown in Fig. 10 and compared with the snow stratigraphy. A detailed discussion is given in section 4.

3.3. Antenna pattern compensation for 3D focusing

A correct interpretation of the generated tomograms must take into account the antenna pattern effect on the recorded backscatter echoes. In our case, the antennas are wideband rectangular horn antennas with apertures of about 40° in both elevation and azimuth directions. To describe the antenna pattern effect, one may consider the complex signal amplitude for a given image position $\vec{r}$ as follows:

$$I(\vec{r}) = \sqrt{K_s}\, e^{i\,\phi_s}\, \sigma(\vec{r}) \otimes h(\vec{r}) + \sqrt{K_n}\, \epsilon(\vec{r}) \tag{15}$$

Here K_s and ϕ_s represent the gain and the phase of the SAR system, $\tilde{\sigma_s}$ is the complex backscatter coefficient at position $\vec{r}$, h is the impulse response of the SAR system and $\otimes$ holds for the convolution operation. The term $\sqrt{K_n}\,\epsilon(\vec{r})$ accounts for additive noise. To be able to compare intensities within the same image, the effect of the system gain must be compensated for. For the AlpSAR data, ϕ_s is considered as null because the system is phase corrected before acquisition by calibrating the VNA and after acquisition by geometrical calibration of antennas positions based on the idea of [25]. Hence, the system gain is expressed by Eq. (16):

$$K_s = \frac{G_{tx}(\theta_{tx}, \phi_{tx})\, G_{rx}(\theta_{rx}, \phi_{rx})\, \lambda^2}{R^4}\, \alpha_s \tag{16}$$

In Eq. (16), $G_{tx}(\theta_{tx}, \phi_{tx})$, $G_{rx}(\theta_{rx}, \phi_{rx})$ are the transmitting and receiving antenna gains, R is the target range and α_s adjusts for all SAR parameters common between all targets. The factor α_s is unknown *a priori* for processed data, hence, it does not affect the comparison between the intensities within the same image. It is worth nothing that the computation of view angles for any target with respect to antenna differs in 3D focusing from 2D focusing. In 3D focusing, the elevation angles $(\theta_{tx}, \theta_{rx})$ to be considered are not the geometrical ones, but those defined after refractive index correction. If the air–medium interface is defined at elevation z_0, the angles θ_{tx}, θ_{rx} will be the out angles of the electromagnetic rays on the surface defined by z_0 (see Fig. 6).

For the synthetic aperture, an average antenna footprint compensation factor over the used antenna positions and frequency bins is computed, resulting in Fig. 7a. Using $\frac{1}{\sqrt{K_s}}$ as the compensation coefficient gives the tomogram of Fig. 7b. The relevant remark here is the artefact out at the limits of the −30 dB aperture of the antenna where the compensation factor is too high. It is clear that the intensity recorded for image pixels where the antenna gain is too low is more likely to be noise and not a meaningful intensity value. A modified compensation factor taking into account the noise level is therefore used to obtain Fig. 8a and 8b:

$$\beta = \frac{\sqrt{K_s}}{K_s + \sigma_n^2} \tag{17}$$

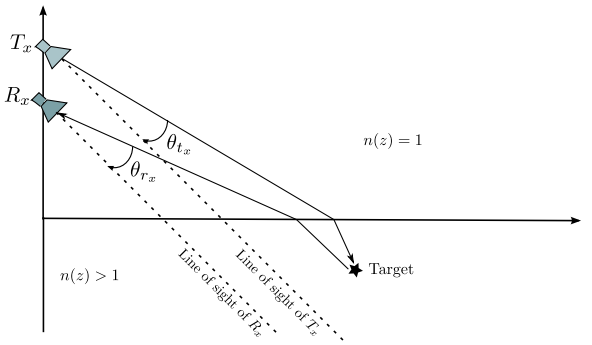

Fig. 6. Definition of the angles accounted for to compute the antenna radiation pattern footprint on the focusing positions.

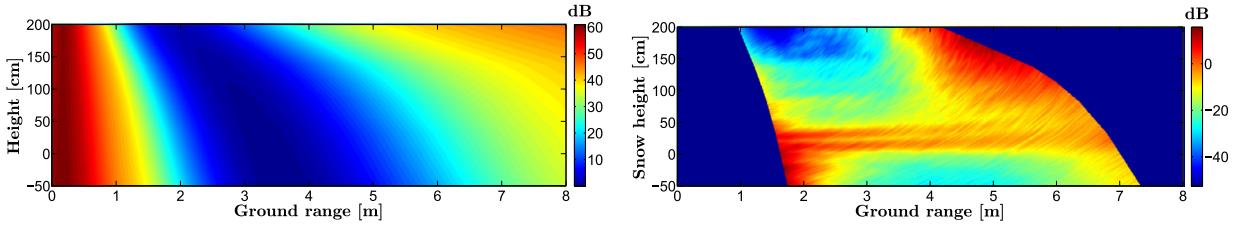

Fig. 7. The panel on the left represents the coefficient $\frac{1}{\sqrt{K_s}}$ used to compensate for the antenna pattern footprint computed after refractive index correction. The panel on the right is the tomogram obtained after antenna footprint compensation. The displayed tomogram is limited over a domain where $\frac{1}{\sqrt{K_s}} <$ 30 dB to avoid that the noise level exceed the signal level.

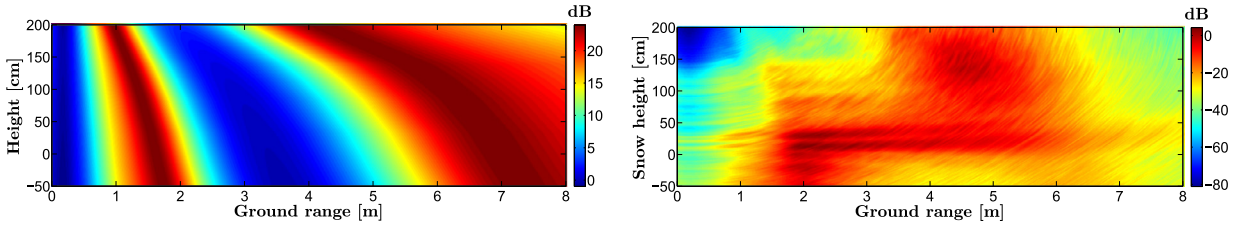

Fig. 8. The panel on the left is the modified compensation coefficient of antenna footprint of Eq. (17) and the panel on the right is the result of application of this coefficient. The used noise level is −30 dB.

Here, σ_n^2 is the adjusting coefficient taking into account the noise level. If K_s is close to one, the compensation factor will be $\beta \approx \frac{1}{K_s} \geq 1$. In this case, a good signal-to-noise ratio is expected and it gives a higher confidence level to the intensity value. Conversely, if K_s is too small compared to σ_n^2, the intensity value is more likely to be noise and it is penalized with a factor $\beta \approx \frac{\sqrt{K_s}}{\sigma_n^2} \leq 1$. The value taken for σ_n^2 is chosen based on the analysis of the raw data, where it is noticed that the noise level is approximatively −30 dB.

4. Interpretation of the results

4.1. Comparing to snow stratigraphy

To compare the obtained tomogram with the snow stratigraphy, the coherency image is exploited since the coherency highlights even coherent backscattering with low intensity. The total snow height observed after correction is less than the total snow height given by the snow stratigraphy (see Fig. 10). The last interface, after correction, is placed at height 15 cm and thus the ground surface is not detected. The snow stratigraphy shows that the first layers are new-fallen dry snow with low densities and small rounded particles. For this kind of snow, the refractive index in the microwave region depends on the snow density and is frequency and temperature independent [21,22]. This explains the low refractive indices found for the first and the second layers (1.1 and 1.2 respectively) where densities are about 150 and 300 kg·m^{-3} for the first and the second layers, respectively. In [22], for dry snow densities ranging from 100 to 400 kg·m^{-3}, refractive indices ranging from 1.10 to 1.30 are found. For deeper layers, the snow wetness, the densities and the grain sizes increase. The snow

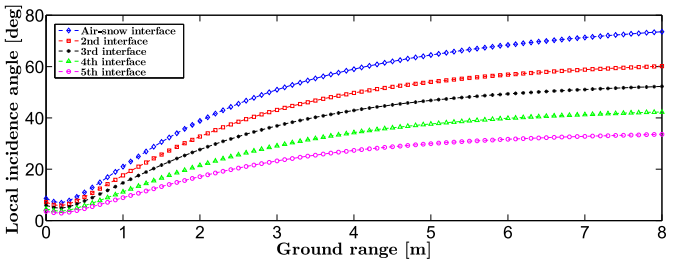

Fig. 9. Local incidence angle computed for the detected interface on the tomogram.

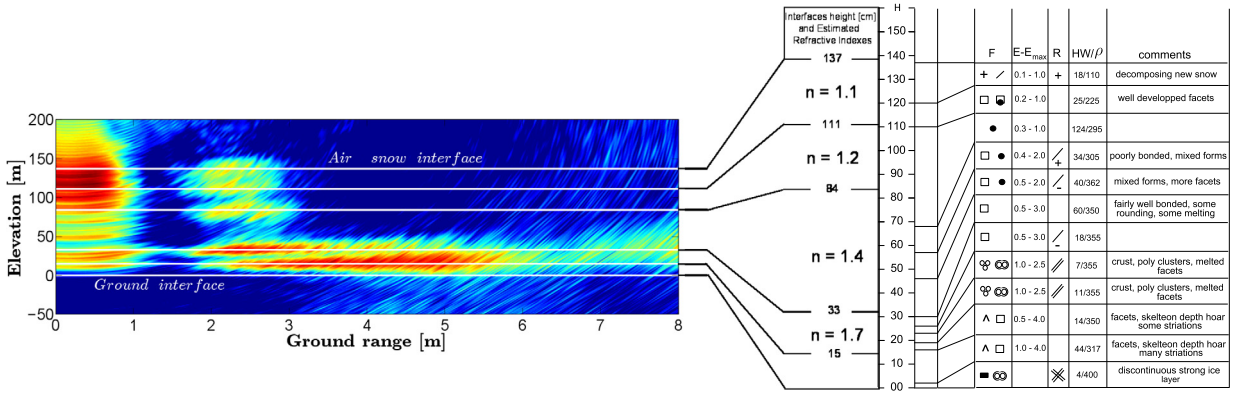

Fig. 10. Obtained tomogram after refractive index correction. The panel on the right is the snow stratigraphy giving different physical parameters of the snowpack as a function of depth. The estimated refractive indices are given for the different layers. For this figure, the antenna pattern is not accounted for.

particles are well-bonded melted forms with poly-clusters. These characteristics explain the higher refractive indices found for the deepest layer snow slabs. The estimated values of refractive indices for the third and the fourth layers are 1.4 and 1.7 respectively. In [21,22], it is shown that the snow refractive index increases with snow wetness and density and ranges from 1.41 to 1.61 at 10 GHz.

Analyzing the height of the detected interfaces and layers, it comes out that the detected interfaces and their positions after correction correspond to changes in the physical parameters of some layers reported on the snow stratigraphy. The second interface is a transition from a layer with a low density and decomposing new-fallen snow into a denser layer with spherical particles. The third interface, within the limits of the resolution of the system, can be considered as the separation between two layers with different particle shapes. The upper one contains mixed forms, while the lower one contains fairly well bonded particles with some melting. The fourth interface, located at 33 cm of snow height, separates an upper snow layer, with fairly bonded melting forms from lower layer with higher wetness, larger grain sizes and more particles aggregates. The last interface defines the last layer with increasing wetness, grain sizes up to 4 mm and depth hoar.

4.2. Backscattered intensity analysis

In Fig. 10, the effect of antenna pattern before compensation can be clearly identified in ground ranges between 1 m and 2 m corresponding to a null between the main lobe and the first side lobe of the antennas. After compensation for the antenna pattern (see Fig. 8b), low backscattered intensities are observed on the shallowest snow interfaces. This can be explained by the low changes in the refractive index as well as the high local incidence angles on these interfaces (see Fig. 9). Indeed, the monostatic backscattering coefficient from a rough surface depends on the incidence angles where higher incidence angles give lower backscattered intensities [26,27]. For deeper interfaces, the high backscattered intensities observed are more likely due to the low local incidence angles on these interfaces. The maximum of the local incidence angle is found to not exceed 42° for the last interface, while it exceeds 72° for the first one.

5. Conclusion

In this work, experimental results of TomSAR applied to snow cover characterization have been presented. The GB-SAR system was operated to characterize the vertical structure of snowpacks. The interfaces between different snow slabs were identified and the influence of free-space propagation assumption for subsurface focusing was highlighted. An iterative procedure was proposed for correcting the focusing process by estimating layer permittivities and thickness of the observed snowpack. For proper interpretation of intensity information, an antenna pattern correction was applied to the tomograms.

The obtained tomograms after index and antenna pattern correction were related to the physical properties of the observed snowpacks. The strongest contributions were found to arise from the deepest snow slabs' interfaces, where the local incidence angles are small. The proposed iterative correction procedure provides a framework to retrieve the physical parameters of the different layers. The results of this work show the great potential of SAR tomography for the characterization of snowpacks and for tuning physical model of electromagnetic interaction with snow.

References

[1] H. Maitre, Processing of Synthetic Aperture Radar (SAR) Images, ISTE, Wiley, 2010.
[2] M.J. Butt, M. Bilal, Application of snowmelt runoff model for water resource management, Hydrol. Process. 25 (2011) 3735–3747.
[3] T. Guneriussen, K. Hogda, K. Sand, ERS-1 SAR for snow monitoring, in: Better Understanding of Earth Environment, Proc. Int. Geoscience and Remote Sensing Symposium, vol. 4, IGARSS '93, 1993, pp. 2008–2010.
[4] J. Shi, J. Dozier, SIR-C/X-SAR investigations of snow properties in Alpine region, in: Quantitative Remote Sensing for Science and Applications, Proc. Int. Geoscience and Remote Sensing Symposium, vol. 2, IGARSS '95, 1995, pp. 1582–1584.
[5] J. Koskinen, J. Pulliainen, M. Hallikainen, The use of ERS-1 SAR data in snow melt monitoring, IEEE Trans. Geosci. Remote Sens. 35 (3) (1997) 601–610.
[6] T. Schellenberger, B. Ventura, M. Zebisch, C. Notarnicola, Wet snow cover mapping algorithm based on multitemporal cosmo-skymed x-band SAR images, IEEE J. Sel. Top. Appl. Earth Obs. Remote Sens. 5 (3) (2012) 1045–1053.
[7] A. Kondoh, N. Kamibayashi, T. Okada, S. Ishimori, S. Fujii, Dependence of radar backscattering coefficient on the water equivalent and other snow conditions at c-band of ERS-1 SAR, in: Better Understanding of Earth Environment, Proc. Int. Geoscience and Remote Sensing Symposium, vol. 3, IGARSS '93, 1993, pp. 1050–1052.
[8] J. Shi, J. Dozier, Estimation of snow water equivalence using SIR-C/X-SAR, in: Remote Sensing for a Sustainable Future, Proc. Int. Geoscience and Remote Sensing Symposium, 1996, vol. 4, IGARSS '96, 1996, pp. 2002–2004.
[9] A. Arslan, J. Koshinen, J. Praks, H. Alasaimi, N. Kruopis, M. Hallikainen, Retrieving snow water equivalence on C- and L-band SAR data for dry snow, in: Proc. IEEE International Geoscience and Remote Sensing Symposium 1998, vol. 4, IGARSS '98, 1998, pp. 1870–1872.
[10] G. Macelloni, M. Brogioni, F. Montomoli, J. Lemmetyinen, J. Pulliainen, H. Rott, Retrieval of snow water equivalent in forested area using multifrequency SAR data, in: Proc. 10th European Conference on Synthetic Aperture Radar, EUSAR 2014, 2014, pp. 1–3.
[11] J. Shi, J. Dozier, Estimation of snow water equivalence using SIR-C/X-SAR. II. Inferring snow depth and particle size, IEEE Trans. Geosci. Remote Sens. 38 (6) (2000) 2475–2488.
[12] S. Leinss, G. Parrella, I. Hajnsek, Snow height determination by polarimetric phase differences in X-band SAR data, IEEE J. Sel. Top. Appl. Earth Obs. Remote Sens. 7 (9) (2014) 3794–3810.
[13] J. Evans, F. Kruse, Determination of snow depth using elevation differences determined by interferometric SAR (INSAR), in: Proc. IEEE International Geoscience and Remote Sensing Symposium 2014, IGARSS, 2014, pp. 962–965.
[14] Z. Li, H. Guo, J. Shi, Estimation of snow density with L-band polarimetric SAR data, in: Proc. IEEE International Geoscience and Remote Sensing Symposium, vol. 4, IGARSS 2000, 2000, pp. 1757–1759.
[15] J. Shi, J. Dozier, Estimation of snow water equivalence using SIR-C/X-SAR. I. Inferring snow density and subsurface properties, IEEE Trans. Geosci. Remote Sens. 38 (6) (2000) 2465–2474.
[16] J. Shi, J. Dozier, H. Rott, Active microwave measurements of snow cover progress in polarimetric SAR, in: Surface and Atmospheric Remote Sensing: Technologies, Data Analysis and Interpretation, Proc. Int. Geoscience and Remote Sensing Symposium, 1994, vol. 4, IGARSS '94, 1994, pp. 1922–1924.
[17] J. Piesbergen, F. Holecz, H. Haefner, Snow cover monitoring using multitemporal ERS-1 SAR data, in: Quantitative Remote Sensing for Science and Applications, Proc. Int. Geoscience and Remote Sensing Symposium, 1995, vol. 3, IGARSS '95, 1995, pp. 1750–1752.
[18] L. Ferro-Famil, C. Leconte, F. Boutet, X. Phan, M. Gay, Y. Durand, Posar: a VHR tomographic GB-SAR system application to snow cover 3-d imaging at X and Ku bands, in: Proc. 9th European Radar Conference, EURAD, 2012, pp. 130–133.
[19] L. Ferro-Famil, S. Tebaldini, M. Davy, C. Leconte, F. Boutet, Very high-resolution three-dimensional imaging of natural environments using a tomographic ground-based SAR system, in: Proc. 8th European Conference on Antennas and Propagation, EuCAP, 2014, pp. 3221–3224.
[20] A. Reigber, A. Moreira, First demonstration of airborne SAR tomography using multibaseline l-band data, IEEE Trans. Geosci. Remote Sens. 38 (5) (2000) 2142–2152.
[21] M. Hallikainen, F. Ulaby, M. Abdel-Razik, Measurements of the dielectric properties of snow in the 4–18 GHz frequency range, in: Proc. 12th European Microwave Conference, 1982, pp. 151–156.
[22] M. Hallikainen, F. Ulaby, M. Abdelrazik, Dielectric properties of snow in the 3 to 37 GHz range, IEEE Trans. Antennas Propag. 34 (11) (1986) 1329–1340.
[23] M. Born, E. Wolf, A. Bhatia, D. Gabor, A. Stokes, A. Taylor, P. Wayman, W. Wilcock, Principles of Optics: Electromagnetic Theory of Propagation, Interference and Diffraction of Light, Cambridge University Press, 2000.
[24] J.A. Sethian, A fast marching level set method for monotonically advancing fronts, Proc. Natl. Acad. Sci. USA 93 (4) (1996) 1591–1595.
[25] S. Tebaldini, M. Mariotti d'Alessandro, F. Banda, C. Prati, Tomographic-quality phase calibration via phase center double localization, in: Proc. IEEE International Geoscience and Remote Sensing Symposium, IGARSS, 2013, pp. 89–92.
[26] J. Zhou, D.-G. Fang, Effective polarized backscattering coefficients of a slightly rough surface to an EM beam, in: Proc. Antennas and Propagation Society International Symposium, 1993, AP-S Digest, vol. 3, 1993, pp. 1320–1323.
[27] C. hao Kuo, M. Moghaddam, Two-dimensional full-wave scattering from discrete random media in layered rough surfaces, in: Proc. IEEE Antennas and Propagation Society International Symposium, 2007, pp. 4801–4804.